Strong Macroscale Supercrystalline Structures by 3D Printing Combined with Self-Assembly of Ceramic Functionalized Nanoparticles

Berta Domènech, Alvin T. L. Tan, Hans Jelitto, Eduardo Zegarra Berodt, Malte Blankenburg, Oliver Focke, Jaclyn Cann, C. Cem Tasan, Lucio Colombi Ciacchi, Martin Müller, Kaline P. Furlan, A. John Hart,* and Gerold A. Schneider*

To translate the exceptional properties of colloidal nanoparticles (NPs) to macroscale geometries, assembly techniques must bridge a 10^6-fold range of length. Moreover, for successfully attaining a final mechanically robust nanocomposite macroscale material, some of the intrinsic NPs' properties have to be maintained while minimizing the density of strength-limiting defects. However, the assembly of nanoscale building blocks into macroscopic dimensions, and their effective macroscale properties, are inherently affected by the precision of the conditions required for assembly and emergent flaws including point defects, dislocations, grain boundaries, and cracks. Herein, a direct-write self-assembly technique is used to construct free-standing, millimeter-scale columns comprising spherical iron oxide NPs (15 nm diameter) surface functionalized with oleic acid (OA), which self-assemble into face-centered cubic (FCC) supercrystals in minutes during the direct-writing process. The subsequent crosslinking of OA molecules results in nanocomposites with a maximum strength of 110 MPa and elastic modulus up to 58 GPa. These mechanical properties are interpreted according to the flaw size distribution and are as high as newly engineered platelet-based nanocomposites. The findings indicate a broad potential to create mechanically robust, multifunctional 3D structures by combining additive manufacturing with colloidal assembly.

To integrate the exceptional properties of nanoscale building blocks into macroscopic devices, manufacturing methods that achieve control of nanoparticle (NP) assembly up to macroscale dimensions have to be developed.[1–8] In this regard, structural hierarchy emerges as a powerful strategy for creating functional materials, involving a precise control of composition and shape across several length scales.[1,9–13]

NPs can be assembled into larger structures by exploiting and further controlling their inherent intermolecular and surface forces.[3,14] Thus, by taking advantage of the short-range forces, colloidal self-assembly appears as a successful bottom-up approach for the development of new materials and their further integration into novel devices. Moreover, by specifically designing the nanobuilding blocks, the macroscopic behavior of the resulting engineered materials can be

Dr. B. Domènech, Dr. H. Jelitto, E. Zegarra Berodt, Dr. K. P. Furlan, Prof. G. A. Schneider
Institute of Advanced Ceramics
Hamburg University of Technology
21073 Hamburg, Germany
E-mail: g.schneider@tu-harburg.de

Dr. A. T. L. Tan, Prof. A. John Hart
Department of Mechanical Engineering
Massachusetts Institute of Technology
02139 Cambridge, MA, USA
E-mail: ajhart@mit.edu

Dr. M. Blankenburg, Prof. M. Müller
Institute of Materials Research
Helmholtz-Zentrum Geesthacht
21502 Geesthacht, Germany

O. Focke
Faserinstitut Bremen e.V.
University of Bremen
28359 Bremen, Germany

O. Focke, Prof. L. Colombi Ciacchi
MAPEX Center for Materials and Processes
University of Bremen
28359 Bremen, Germany

J. Cann, Prof. C. Cem Tasan
Department of Materials Science and Engineering
Massachusetts Institute of Technology
02139 Cambridge, MA, USA

Prof. L. Colombi Ciacchi
Hybrid Materials Interfaces Group
Faculty of Production Engineering
Bremen Center for Computational Materials Science
University of Bremen
28359 Bremen, Germany

specifically tuned. Typically, self-assembly is used for obtaining 1D or 2D structures whereas the design of 3D materials and structures is still in its infancy.[15–20] But, if colloidal self-assembly is combined with a 3D printing technique, the long-range tailor-made design of material systems could be achieved.

Direct ink writing (also named robocasting)[21–23] is a 3D printing technique in which ink is supplied to a needle or nozzle and it is extruded continuously or at intervals, while moving in relation to the substrate. A shear thinning ink must flow through the needle aperture under stress and yet have shape retention capability upon deposition. Therefore, the development and optimization of inks with myriad constituents ranging from metal-based to biomaterials are objects of extensive research.[24] Recently, it was demonstrated that macroscale polycrystalline colloidal structures of polystyrene, silica, and gold particles (diameters from 80 to 1000 nm) could be built using a colloidal suspension instead of a shear thinning ink in direct-write 3D printing.[23]

For most applications, though, the successful bridging of several length scales depends on the intrinsic mechanical robustness of synthesized nanocomposites.[1] Although NPs are ultra-strong up to their theoretical strength,[9] for obtaining a mechanically strong nanocomposite, the bonding forces between NPs must be in the order of several hundreds of MPa. Thus, new strategies that allow combining hierarchical assembly, starting at the nanoscale, with mechanical robustness of the final material, are required. In previous publications, we demonstrated that the colloidal assembly of NPs surface functionalized with hydrocarbon ligands and the

further crosslinking of the organic phase at temperatures lower than 400 °C can deliver materials with exceptional mechanical properties when tested at the microscale.[25–27] Unfortunately, the nanocomposites obtained by this macroscopic self-assembly process comprised several macroscopic cracks, which reduced their mechanical strength down to values as low as 10 MPa.

In this study we combine direct-write 3D printing with the colloidal self-assembly of 15 nm iron oxide NPs (Fe_3O_4-NPs), surface functionalized with organic ligands (oleic acid, OA), to fabricate free-standing mechanically robust macroscale supercrystalline structures in a facile and fast route.

The direct-write colloidal assembly was conducted using a custom-fabricated bench-top direct-writing system (**Figure 1**A and Figure S2, Supporting Information).[23] In this setup, a toluene-based suspension of OA-functionalized Fe_3O_4-NPs (see Figure S1, Supporting Information) is dispensed from a high-precision needle onto a substrate, forming a liquid bridge. During the colloidal assembly process, the liquid bridge provides confinement for the NPs that accumulate at the base and form the self-assembled solid column. As presented in the in situ real-time column fabrication video (Video S1, Supporting Information), the process is controlled by moving the substrate downward at a rate matched to the vertical growth rate of the self-assembled printed column. More information on the writing process can be found in the Supporting Information section. By this process, free-standing millimeter-sized columns (Figure 1B) with a super-crystalline structure (Figure 1C) are produced.
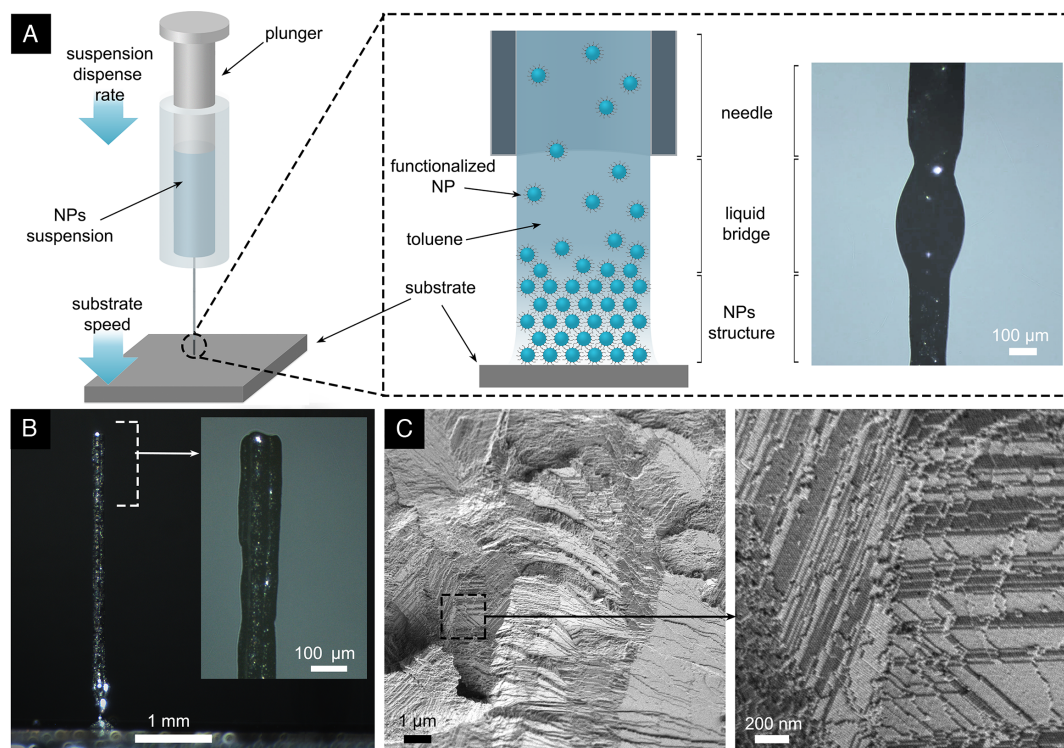
Figure 1. A) The 3D printing colloidal assembly is performed by dispensing the colloidal suspension from a high-precision needle, followed by controlled downward motion of the substrate and syringe plunger. This allows the construction of free-standing mm-sized columns such as the one presented in the B) digital photograph. C) High-resolution SEM images of the cross section of one column revealing the ordered arrangement of NPs and grain boundaries between the micron-sized supercrystalline grains.
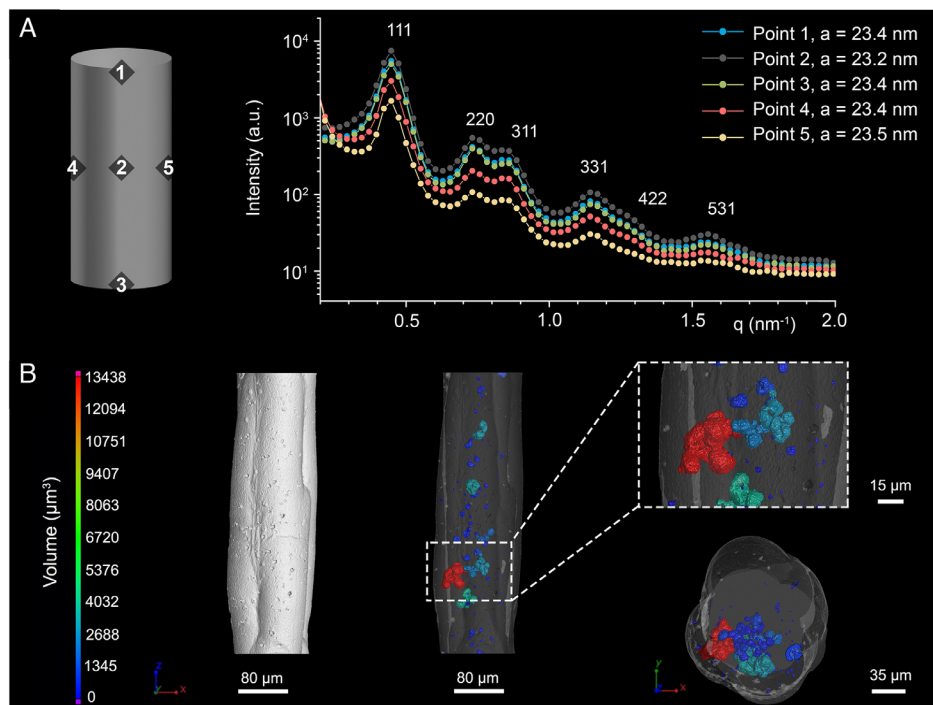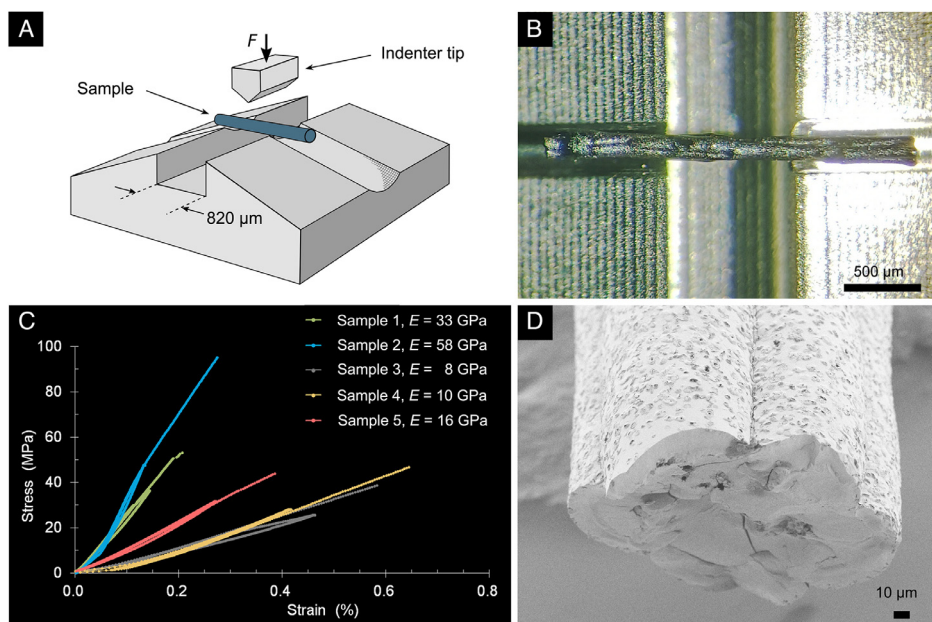
Figure 2. A) Schematic drawing of a 3D-printed column with different highlighted positions from where the SAXS 2D scattering curves with the indexed peaks and the corresponding lattice parameters (a) are presented. The distance between point 1 and 3 (vertical scan) is 2.2 mm, the distance between point 4 and 5 (horizontal scan) is 0.2 mm. More information can be found on Chapter 3, Supporting Information. A,B) XRM 3D reconstruction of a 3D-printed free-standing column and corresponding porosity evaluation. From left to right: Outer structure of the column (3D view), color-coded volume size of internal voids, and the corresponding enlarged 3D lateral and longitudinal (cross-section) views. The flower-like cross section is visualized in the bottom-left part of the figure, together with the asymmetric location of the voids. XRM reconstruction videos of the sample are available as Supplementary Information videos (SI Videos 2 and 3, Supporting Information).

To evaluate and discern possible variations in the superlattices forming the samples, synchrotron-based small-angle X-ray scattering (SAXS) analyses were conducted at different points along the columns axes, both vertically and in the cross section (horizontally). As shown in **Figure 2**A, regardless of the sample position, a face-centered cubic (FCC) superlattice was identified. Moreover, no significant differences were detected for the lattice parameter as a function of the column position (see Figure S3, Supporting Information), allowing us to calculate a mean lattice parameter of 23.3 nm, nearest neighbor distance of 16.5 nm, and interparticle distance of 1.3 nm. Such short interparticle distances—shorter than a ligand molecule ($\approx$ 2 nm)[18,25,27]—indicate that the OA molecules between adjacent NPs are interdigitated. This is in fact an important requisite for the system, as it allows the organic ligands to be further crosslinked during the subsequent thermal annealing, resulting in an enhancement of the material's mechanical response.[25–27]

X-ray microscopy (XRM) was applied to a piece of a 3D-printed column with a total length of 460 µm. The 3D reconstruction of the data and further image analysis allowed the detection of asymmetrically distributed internal voids and pores inside the column (Figure 2B), accounting for a total volume of 41 311 µm³, which corresponds to 0.6% of the samples' evaluated total volume. The equivalent spherical diameter of the pores has a mean value of 7 µm, largest value of 45 µm, and smallest value of 2 µm. The XRM 3D reconstruction also revealed a flower-like cross section,

which is hypothesized to form during the drying step. Initially, the column is formed as a wet solid in the bottom of the liquid bridge. In the wet state, there is steric repulsion between the surface organic ligands and thus more spacing between suspended NPs.[14] Solvent evaporation proceeds at the free surface (liquid–gas interface) and the driving force for solvent diffusion to the surface is the capillary pressure. As the solvent evaporates, NPs are forced into contact by the capillary pressure of receding menisci. As a result of surface drying, a ring of highly packed assembled NPs forms on this external region, whereas the core maintains less packed NPs remaining in suspension. Once the outer ring reaches a critical point where it cannot shrink anymore, a shape change—from a circular cross section to flower-like cross section—occurs to enable the inner core to reduce its cross-sectional area while keeping the circumference of the outer ring constant. Also, as a result of the restriction of the rigid self-assembled column's surface to accommodate the volume reduction, internal voids arise, as observed by XRM (Figure 2B). Ongoing optimizations of the 3D printing process are tackling these issues by, e.g., increasing the stability of the liquid bridge by tailoring the substrate–suspension interactions and exerting a more precise control of the solvent vapor pressure at the liquid bridge and column's surroundings.

After direct-write assembly, the OA molecules at the interfaces between the ceramic NPs that form the columns' superlattices were crosslinked by heat treatment at 325 °C. The annealed columns were further tested via three-point bending, as shown in

ADVANCED
SCIENCE NEWS
www.advancedsciencenews.com

ADVANCED
ENGINEERING
MATERIALS
www.aem-journal.com

Figure 3. A) Schematic drawing of the bending device, showing the lower support with the columnar sample and the nanoindenter wedge. B) Photograph of a sample lying on the support used for bending tests. C) Force displacement curves with loading and unloading cycles of five different samples. The samples were measured until fracture. D) SEM image of a typical fracture surface of a heat-treated column after the bending test.

Figure 3A and Figure 3B. The load-displacement curves of several samples shown in Figure 3C indicate that, in addition to the initial adjustment period, all the different 3D-printed heat-treated columns tested show a linear elastic behavior until final fracture. The further scanning electron microscopy (SEM) evaluation of the obtained fracture surfaces confirmed the NPs' periodic arrangement (Figure S5, Supporting Information) throughout the columns' cross sections, ruling out the possibility of the fracture starting point being an amorphous region but rather pointing out to the micron-sized defects identified by XRM, as shown in the SEM image (Figure 3D).

The elastic modulus of the different crosslinked columns varies between 8 and 58 GPa and the bending strength between 39 and 110 MPa (details in Supporting Information, Section 5). Such a variation is attributed to the pore size distribution and the asymmetric location of the pores inside the columns, which locally change the moment of inertia depending on the location of the pores in the loaded column's cross section. To the best of the authors' knowledge, the values hereby presented are the highest ever reported for supercrystalline materials of these sizes, in the millimeter range, reaching the elastic modulus and strength of natural enamel.[28] Furthermore, and as discussed later (**Figure 4**A,B), the strengths of these materials favorably compare with newly engineered brick-and-mortar hierarchical composite materials.[28–32]

The mechanical strength of 10–100 nm-sized ceramic NPs is usually of the order 1/30 of their elastic modulus E.[9] Hence, for the NPs used in this study—E of 163 GPa[33]—the theoretical strength is ≈ 5 GPa. For hybrid organic–inorganic nanocomposite materials, though, the maximum strength of the final nanocomposite is determined by the interface strength between the organic and inorganic phase (ligand–NPs, here) or by the strength between the organic molecules. In a previous work, we showed that the strength of the supercrystals is determined by the strength of the crosslinked OA (σ_{OA}), which relates to the force of one OA molecule (F_{OA}) via the crosslink area density ρ_{cl}, as $\sigma_{OA} = F_{OA}\rho_{cl}$. From this, $F_{OA} \cong 2$ nN arises.[25] Therefore, with a crosslink density of $\rho_{cl} \cong 0.45$ nm^{-2},[25] a maximum strength of $\sigma_{SCmax} = 900$ MPa is obtained. This value of σ_{SCmax} accounts for the maximum possible strength, assuming a defect-free supercrystalline nanocomposite (dashed line in Figure 4A). As the supercrystals investigated here consist of spherical NPs, shear forces play a minor role in transferring load via the organic phase. Thus, toughening due to the nonlinear shearing of the organic phase at its yield strength—resulting in nanovoids and a quasiplastic behavior typical of nacre-like materials—is not expected to occur.[34]

The supercrystals are brittle with a fracture toughness of $K_{Ic} = 0.35 \pm 0.15$ MPa $\sqrt{m}$.[26] For increasing the size of supercrystals, a transition between σ_{SCmax} and a defect size a controlling the strength of the poly-supercrystals (σ_{SC}) is expected. This can be described by the well-known Griffith equation $\sigma_{SC} = K_{Ic}/\sqrt{\pi a}$. Note that, as we focus on scaling properties, the complex 3D geometry of the cracks is neglected; thus, surface cracks of length a are considered (details in Supporting Information, Chapter 7). As already discussed by Gao et al.[9] the defect size typically scales linearly with the thickness d of the samples (diameter of the columns, in this case) as $a \propto d$. As shown in Figure 4A, the strongest 3D-printed columns here reported correspond to a defect size of $a \approx 0.03d$, thus 4 μm. On the other hand, for the weaker columns, the fracture mechanics calculation delivers $a \approx 0.1d = 16$ μm. Both values are in agreement with the measured maximum and minimum void diameters (45 and 2 μm, respectively) determined by XRM, taking into
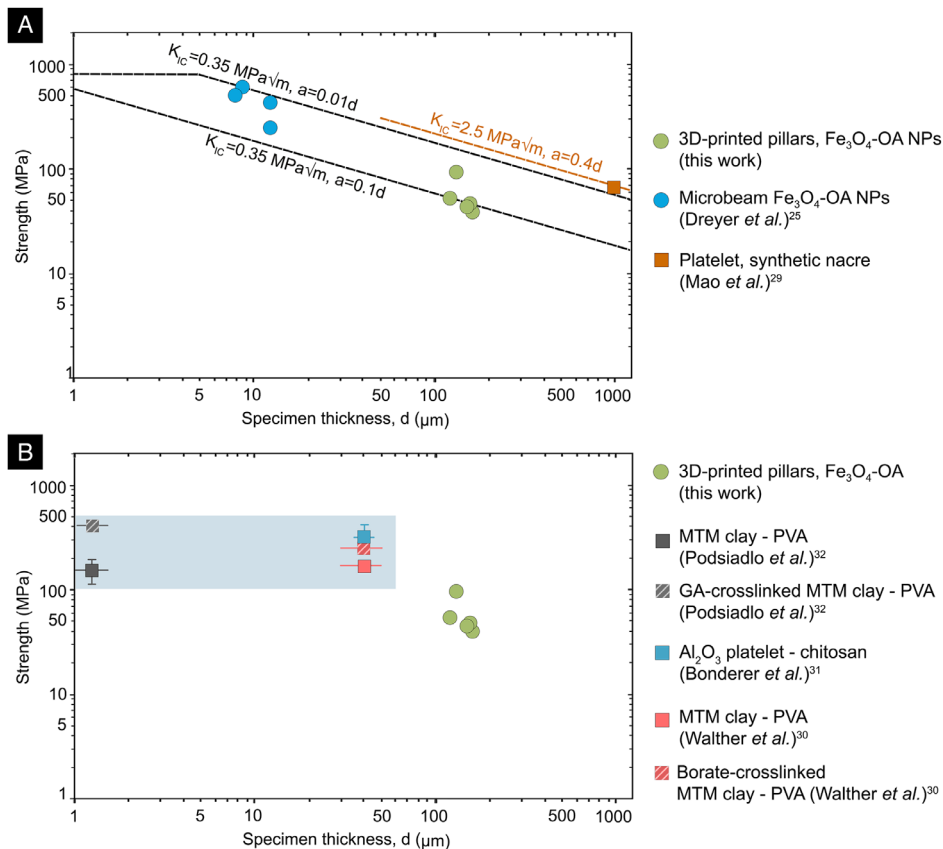
Figure 4. Measured strength of supercrystalline and nacre-like nanocomposites as a function of the specimen thickness. A) A comparison of the bending strength of 3D-printed crosslinked supercrystalline columns with microbending bars obtained on a similar material (OA-functionalized Fe_3O_4-NPs)[25] and macroscopic synthetic nacre.[29] These composites are defect size controlled, showing brittle fracture. B) Tensile strength of nanoplatelet-based brick-and-mortar composites[30–32] controlled by the shear strength of the organic phase. As a consequence, these composites are not defect controlled and their strength is constant at least up to 50 µm specimen thickness, indicated by the rectangular region highlighted in blue. For comparison, the strength of the here-reported 3D-printed supercrystalline columns is also presented. Notice that the specimen thickness is much higher in this work than previous reports.

account that in 3-point bending the maximum stress arises at the center of the structure, where, as shown by XRM, it is unlikely that the largest void is placed. Interestingly, previously investigated 5 µm-thick microbeams from a similar material (self-assembled by a classical bottom-up method)[25] show the same scaling behavior, where the best microbeam samples present defect sizes in the order of 100 nm.

For additional comparison, a macroscopic millimeter-thick synthetic nacre-like hierarchical composite of platelet-shaped aragonite grains (diameter ≈ 36 µm and thickness ≈ 5 µm) consisting of nanograins (diameters from 10 to 100 nm)[29] is also shown in Figure 4A. Even though this nacre-like nanocomposite material has a fracture resistance curve with an initial fracture toughness of $1.6\,MPa\sqrt{m}$, rising to about $2.5\,MPa\sqrt{m}$ after 200 µm crack extension, it is found to fail by brittle fracture. Thus, the measured three-point bending strength of these nacre-like nanocomposites (of 64 MPa) can be associated with crack-like defects with $a = \frac{1}{\pi}\left(\frac{K_{Ic}}{\sigma_c}\right)^2 = \frac{1}{\pi}\left(\frac{2.5\,MPa\sqrt{m}}{64\,MPa}\right)^2 = 400\,\mu m = 0.4d$ (orange line in Figure 4A), which is in the same range as the defect size found in our supercrystalline columns.

Figure 4B shows a comparison of the strengths of different nacre-like organic-inorganic composites reported in literature.[30–32] These nacre-like composites show strengths between 110 and 400 MPa and are based on nanometer-thick montmorillonite (MTM) clay or 200 nm-thick alumina platelets, assembled to cm-sized films via layer-by-layer assembly[31,32] or by paper-making mimetic processes.[30] For those nanocomposites including a further crosslinking of the organic phase, their strengths increased,[30,32] indication that the shear strength of the polymer controls the strength of the final nanocomposite, at least for thicknesses smaller than 50 µm. Consequently, their strength is constant up to a sample thickness of 50 µm. The maximum strength of the 3D-printed crosslinked columns (110 MPa) reaches the strength of these nanoplatelet-based nanocomposites, forecasting their exceptional potential, even in the absence of the shear stress transfer mechanism present in platelet-based nanocomposites.

Thus, with this work, we demonstrate that the combination of colloidal assembly with 3D printing enables the facile and fast fabrication of robust millimeter-long columns, bridging almost five different length scales. The simple concept of covalently

linking hard inorganic NPs in a well-ordered superstructure by soft organic molecules is successfully transferred from classical self-assembly techniques to a direct-writing process. As a long-term perspective, we envisage that this combination of 3D printing and self-assembly will lead to novel macroscopic material architectures, allowing the design of unprecedented multifunctional devices.

Experimental Section

Experimental Section details are in Supporting Information.

Supporting Information

Supporting Information is available from the Wiley Online Library or from the author.

Conflict of Interest

The authors declare no conflict of interest.

[1] M. R. Begley, D. S. Gianola, T. R. Ray, *Science* **2019**, *364*, 1.
[2] E. V. Sturm, H. Cölfen, *Crystals* **2017**, *7*, 207.
[3] M. A. Boles, M. Engel, D. V. Talapin, *Chem. Rev.* **2016**, *116*, 11220.
[4] A. S. Baimuratov, I. D. Rukhlenko, V. K. Turkov, A. V. Baranov, A. V. Fedorov, *Sci. Rep.* **2013**, *3*, 1.
[5] S. C. Glotzer, M. J. Solomon, *Nat. Mater.* **2007**, *6*, 557.
[6] M. P. Pileni, *J. Phys. Chem. B* **2001**, *105*, 3358.
[7] T. Tachikawa, T. Majima, *NPG Asia Mater.* **2014**, *6*, 1.
[8] B. Domènech, M. Kampferbeck, E. Larsson, T. Krekeler, B. Bor, D. Giuntini, M. Blankenburg, M. Ritter, M. Müller, T. Vossmeyer, H. Weller, G. A. Schneider, *Sci. Rep.* **2019**, *9*, 1.
[9] H. Gao, B. Ji, I. L. Jager, E. Arzt, P. Fratzl, *PNAS USA* **2003**, *100*, 5597.
[10] M. Eder, S. Amini, P. Fratzl, *Science* **2018**, *362*, 543.
[11] Y. A. Shin, S. Yin, X. Li, S. Lee, S. Moon, J. Jeong, M. Kwon, S. J. Yoo, Y.-M. Kim, T. Zhang, H. Gao, S. H. Oh, *Nat. Commun.* **2016**, *7*, 1.
[12] Z. Qin, M. J. Buehler, *Nanotechnology* **2018**, *29*, 280201.
[13] G. X. Gu, M. Takaffoli, M. J. Buehler, *Adv. Mater.* **2017**, *29*, 1.
[14] M. Gerth, I. K. Voets, *Chem. Commun.* **2017**, *53*, 4414.
[15] Z. Xue, C. Yan, T. Wang, *Adv. Funct. Mater.* **2019**, *29*, 1807658.
[16] K. P. Furlan, E. Larsson, A. Diaz, M. Holler, T. Krekeler, M. Ritter, A. Y. Petrov, M. Eich, R. Blick, G. A. Schneider, I. Greving, R. Zierold, R. Janßen, *Appl. Mater. Today* **2018**, *13*, 359.
[17] C. Hanske, E. H. Hill, D. Vila-Liarte, G. González-Rubio, C. Matricardi, A. Mihi, L. M. Liz-Marzán, *ACS Appl. Mater. Interfaces* **2019**, *11*, 11763.
[18] M. C. Weidman, Q. Nguyen, D.-M. Smilgies, W. A. Tisdale, *Chem. Mater.* **2018**, *30*, 807.
[19] J. Wang, U. Sultan, E. S. A. Goerlitzer, C. F. Mbah, M. Engel, N. Vogel, *Adv. Funct. Mater.* **2019**, *1907730*, 1.
[20] P.-p. Wang, Q. Qiao, Y. Zhu, M. Ouyang, *J. Am. Chem. Soc.* **2018**, *140*, 9095.
[21] M. K. Hausmann, P. A. Rühs, G. Siqueira, J. Läuger, R. Libanori, T. Zimmermann, A. R. Studart, *ACS Nano* **2018**, *12*, 6926.
[22] Y. Cheng, K. H. Chan, X.-Q. Wang, T. Ding, T. Li, X. Lu, G. W. Ho, *ACS Nano* **2019**, *13*, 13176.
[23] A. T. L. Tan, J. Beroz, M. Kolle, A. J. Hart, *Adv. Mater.* **2018**, *30*, e1803620.
[24] E. Peng, D. Zhang, J. Ding, *Adv. Mater.* **2018**, *30*, e1802404.
[25] A. Dreyer, A. Feld, A. Kornowski, E. D. Yilmaz, H. Noei, A. Meyer, T. Krekeler, C. Jiao, A. Stierle, V. Abetz, H. Weller, G. A. Schneider, *Nat. Mater.* **2016**, *15*, 522.
[26] B. Bor, D. Giuntini, B. Domènech, M. V. Swain, G. A. Schneider, *J. Eur. Ceram. Soc.* **2019**, *39*, 3247.
[27] B. Domènech, A. Plunkett, M. Kampferbeck, M. Blankenburg, B. Bor, D. Giuntini, T. Krekeler, M. Wagstaffe, H. Noei, A. Stierle, M. Ritter, M. Müller, T. Vossmeyer, H. Weller, G. A. Schneider, *Langmuir* **2019**, *35*, 13893.
[28] S. Bechtle, S. F. Ang, G. A. Schneider, *Biomater.* **2010**, *31*, 6378.
[29] L.-B. Mao, H.-L. Gao, H.-B. Yao, L. Liu, H. Cölfen, G. Liu, S.-M. Chen, S.-K. Li, Y.-X. Yan, Y.-Y. Liu, S.-H. Yu, *Science* **2016**, *354*, 107.
[30] A. Walther, I. Bjurhager, J.-M. Malho, J. Pere, J. Ruokolainen, L. A. Berglund, O. Ikkala, *Nano Lett.* **2010**, *10*, 2742.
[31] L. J. Bonderer, A. R. Studart, L. J. Gauckler, *Science* **2008**, *319*, 1069.
[32] P. Podsiadlo, A. K. Kaushik, E. M. Arruda, A. M. Waas, B. S. Shim, J. Xu, H. Nandivada, B. G. Pumplin, J. Lahann, A. Ramamoorthy, N. A. Kotov, *Science* **2007**, *318*, 80.
[33] H. J. Reichmann, S. D. Jacobsen, *Am. Mineral.* **2004**, *89*, 1061.
[34] U. G. K. Wegst, H. Bai, E. Saiz, A. P. Tomsia, R. O. Ritchie, *Nat. Mater.* **2015**, *14*, 23.